Applied Surface Science 475 (2019) 312–324

Contents lists available at ScienceDirect

Applied Surface Science

journal homepage: www.elsevier.com/locate/apsusc

Full Length Article

MnO_x/Cr_2O_3 composites prepared by pyrolysis of Cr-MOF precursors containing *in situ* assembly of MnO_x as high stable catalyst for toluene oxidation

Xi Chen[a,b], Xi Chen[a,b], Songcai Cai[a,b], Enqi Yu[a,b], Jing Chen[b,c,d], Hongpeng Jia[a,b,*]

[a] CAS Center for Excellence in Regional Atmospheric Environment, and Key Laboratory of Urban Pollutant Conversion, Institute of Urban Environment, Chinese Academy of Sciences, Xiamen 361021, China
[b] University of Chinese Academy of Sciences, Beijing 100049, China
[c] Xiamen Institute of Rare-earth Materials, Haixi Institutes, Chinese Academy of Sciences, Xiamen 361021, China
[d] Fujian Institute of Research on the Structure of Mater, Chinese Academy of Sciences, Fuzhou 350002, China

ARTICLE INFO

Keywords:
Manganese/chromium oxide
Pyrolysis
MOFs
Catalytic oxidation
VOCs

ABSTRACT

A series of MnO_x/Cr_2O_3 composites have been prepared *via* the combination methods of impregnation, *in situ* redox precipitation and pyrolysis based on MIL-101-Cr. The physicochemical properties of catalysts have been investigated by using XRD, Raman, BET, SEM, TEM, XPS, H_2-TPD and O_2-TPD, and their catalytic performance has been evaluated by toluene combustion. With introduction of MnO_x into Cr_2O_3, the MnO_x/Cr_2O_3-M exhibits the obviously enhanced catalytic activity for toluene oxidation compared to commercial Cr_2O_3 or pure Cr_2O_3 pyrolyzed by MIL-101-Cr. The 14.6 wt% MnO_x/Cr_2O_3-M (named as $15Mn/Cr_2O_3$-M) shows the highest efficiency and lowest E_a values under different SV and toluene concentrations. The catalytic durability test for toluene oxidation on $15Mn/Cr_2O_3$-M presents a solid stability, where the toluene conversion maintains at ca. 85% for at least 240 h without obvious inactivation (270 °C, 1000 ppm of toluene, 20,000 mL/(g h), with 10 vol% of water vapor) and it can also maintain at conversions of 90% and 50% for at least 50 h with higher space velocity (1000 ppm of toluene, 60,000 mL/(g h)). The good durability and tolerance of $15Mn/Cr_2O_3$-M are probably associated with better stability for crystal structure, oxygen vacancies, and reducibility. More MnO_x addition amount ($25Mn/Cr_2O_3$-M) cannot further promote catalytic performance, possibly due to excessive MnO_x existed as isolated phase with lack of strong interaction between two metal oxides. The investigation of *in situ* DRIFTS on $15Mn/Cr_2O_3$-M confirms that surface lattice oxygen O_{Latt} plays a crucial role in toluene combustion and the pathway for toluene combustion is *via* rapid transformation to aldehydic and then benzoate species and finally form CO_2 and H_2O.

1. Introduction

Volatile organic compounds (VOCs) have become a severe trouble to environment and public health, which mainly emit from industrial processes and human activities [1,2]. And various techniques have been applied to the abatement of VOCs. Among them, catalytic combustion is considered as the most efficient and practical technology for the removal of a majority of VOCs due to no harmful byproducts in the process and its relatively low temperature in actual application [3–5]. The key issue of such a technology is the development of catalysts with high performance. Considering the economic cost, non-noble metal catalysts such as transition metal oxides have gained much attention for the characteristics of lower cost and less secondary pollution [6,7]. A large of metal oxide catalysts have been successfully used for degradation of different VOCs [5,8–15]. Among the alternative transition metal oxides, MnO_x exhibited a comparable activity to noble-metal catalysts in the removal of gaseous pollutants due to the abundant oxygen species and good reducibility derived from its polymorphism and polyvalence [16–18]. Even so, the sole MnO_x is still hard to satisfy the catalytic performance in terms of structural thermostability and activity to some kind of VOCs. Additionally, Cr_2O_3 is often chosen as catalyst for the better thermostability and anti-poisoning to oxidation of organics [19–23], but weak oxygen mobility inhibits its developments of practical applications for VOCs catalytic removal [24–27]. Thus, an

* Corresponding author at: CAS Center for Excellence in Regional Atmospheric Environment, and Key Laboratory of Urban Pollutant Conversion, Institute of Urban Environment, Chinese Academy of Sciences, Xiamen 361021, China.
E-mail address: hpjia@iue.ac.cn (H. Jia).

https://doi.org/10.1016/j.apsusc.2018.12.277
Received 25 October 2018; Received in revised form 17 December 2018; Accepted 29 December 2018
Available online 31 December 2018
0169-4332/

effective strategy is to develop mixed metal oxides (MMOs) catalysts by multi-metal combination for VOCs catalytic combustion, which provides possibly complementary advantages of different metals to make up the deficiency of catalytic performance for single metal oxide [2,25]. For example, the introduction of the second metal ions (Ce, Fe, Co, Cu, etc.) into Mn-based oxides has shown obvious influence on catalytic performance of VOCs combustion [2,25,28,29]. Chen, et al. reported Mn-Cr mixed oxides were more active than individual manganese and chromium oxides in catalytic removal of NO_x, which benefited from the properties of two metal oxides and unique synergistic effect [30]. On the other hand, the catalytic performance of catalysts is tightly related to the intrinsic nature such as structure and physicochemical properties, which can be probably improved by various preparation methods (co-precipitation, sol-gel, template and impregnation method) [28,31,32]. Recently, a new effective method to synthesize metal oxides via pyrolysis of metal-organic frameworks (MOFs) has exhibited enhanced physicochemical properties, which is believed to be beneficial to promote catalytic efficiency for VOCs oxidation [33–35]. Notably, it has been verified by us to be an effective preparation method for pure metal oxides or noble metal supported catalysts with enhanced catalytic performance of VOCs degradation [5,36].

Inspired by the above mentioned, the binary oxides MnO_x/Cr_2O_3 composites with different mass ratio of MnO_x and Cr_2O_3 were successfully synthesized using MOF (MIL-101-Cr) as the template. With the help of several characterization analysis, the catalysts labeled 15Mn/Cr_2O_3-M presented the best catalytic activities, improved stability and water vapor resistant, which provided a promising synthetic route for high-efficient catalyst of VOCs degradation based on MOF-template. The better catalytic performance and thermostability is mainly due to the synergistic effect of MnO_x and Cr_2O_3.

2. Experimental section

2.1. Chemicals and materials

All the reagents (A.R. grade) were used directly without further purification. 1,4-dicarboxybenzene (99%) was purchased from Aladin (China, Shanghai). Commercial Cr_2O_3 (Cr_2O_3-C), HF (40 wt% in H_2O), $Cr(NO_3)_3{\cdot}9H_2O$ (99%), $KMnO_4$, H_2O_2 (30 wt% in H_2O), and ethanol were purchased from Sinopharm Chemical Reagent Co., Ltd (China, Shanghai).

2.2. Preparation of MIL-101-Cr

MIL-101-Cr was prepared by a hydrothermal process as described in our previous report with modification [5]. Typically, a mixture containing 4 g of $Cr(NO_3)_3{\cdot}9H_2O$, 1.66 g of 1,4-dicarboxybenzene, 0.5 mL of HF and 70 mL of H_2O was treated under ultrasonication for 1 h and then stirred for 2 h. Subsequently, the resulting solution was transferred into a Teflon-lined stainless-steel autoclave and heated at 220 °C for 8 h. After hydrothermal process, the precipitates were collected and washed with ethanol and water for several times. The obtained powders were re-dispersed in 100 mL of ethanol in an autoclave and heated at 100 °C for 24 h to further purify. Finally, the product was collected, dried in an oven at 100 °C overnight.

2.3. Preparation of x MnO_x/Cr_2O_3-M

500 mg of MIL-101-Cr was dispersed in 100 mL H_2O under ultrasonication and a solution containing desired amount of $KMnO_4$ (theoretical addition amounts are determined by 10, 20, and 30 wt% loading weights of MnO_x produced from $KMnO_4$, which is calculated based on the obtained Cr_2O_3 derived from MIL-101-Cr) was added dropwise to the above suspension with vigorous stirring. After stirring for the other 2 h, 3 mL H_2O_2 diluted in 50 mL H_2O was added dropwise to the mixture and was continuously stirred for 1 h. The sample was filtered off, washed with water, and dried at 80 °C for 2 h. Finally, the precursors were calcined at 500 °C for 2 h under air with the heating rate of 2 °C/min. Determined by ICP-OES analysis (actual contents of Mn: 4.8 wt%, 14.6 wt%, 25.4 wt%), the products were donated as the 5Mn/Cr_2O_3-M, 15Mn/Cr_2O_3-M, 25Mn/Cr_2O_3-M, respectively, and the corresponding precursors of the catalysts were named as 5Mn/MIL-101-Cr, 15Mn/MIL-101-Cr, and 25Mn/MIL-101-Cr, respectively.

2.4. Preparation of Cr_2O_3-M

As a reference catalyst, Cr_2O_3-M was synthesized under the same conditions with x MnO_x/Cr_2O_3-M except no addition of Mn source. 500 mg of MIL-101-Cr was dispersed in 100 mL H_2O under ultrasonication and 3 mL H_2O_2 diluted in 50 mL H_2O was added dropwise to the suspension with continuous stirring for 1 h. It was accordance with the preparation process of MnO_x/Cr_2O_3-M, which guaranteed the catalytic activities of samples were not influenced by any other factors. The sample was filtered off, washed with water, and dried at 80 °C for 2 h. Then, the obtained samples were treated under air at 500 °C for 2 h with the heating rate of 2 °C/min to finally form Cr_2O_3-M.

2.5. Catalytic test

Catalytic activity was carried out on fixed bed reactor with a quartz tube of 6 mm of inner diameter at atmospheric pressure. 0.1 g of the obtained catalysts without any further treatment (40–60 mesh) were loaded on the reaction bed. The feed flow rates were set at 33.3, 100, or 200 mL/min and gave the SV of 20,000, 60,000 or 120,000 mL/(g h), respectively. Air flow containing 1000 ppm of toluene was passed through the reactor from top to bottom, where toluene vapor was controlled by blowing dry air into a liquid toluene saturator. Reaction temperatures were measured at the bottom of bed layer. Toluene conversions were calculated based on CO_2 yield. The influence of water vapor to catalytic activity over catalysts was investigated by introducing 5 vol% or 10 vol% H_2O into the feed flow using a water saturator at certain temperature. The outlet gas stream was analyzed online by a gas chromatograph equipped with a nickel catalysis transition furnace and two flame ionization detectors (FID). The catalytic performance of catalyst was conducted, where $T_{10\%}$, $T_{50\%}$, $T_{90\%}$ of reaction temperatures were referred to 10, 50, 90% of toluene conversions. In catalytic test process, only CO_2 was detected, which indicates the complete decomposition of toluene over these catalysts.

2.6. Durability tests

The catalytic durability was performed on 15Mn/Cr_2O_3-M under the following conditions: (1) toluene conversions were retained at around 50 and 90% at corresponding temperatures for 50 h, respectively (toluene concentration = 1000 ppm and SV = 60,000 mL/(g h)); (2) Water tolerance on catalytic activity was tested by 5 and 10 vol% of water vapor for 12 h, respectively (toluene concentration = 1000 ppm and SV = 60,000 mL/(g h)); (3) For potential practical application, 10 vol% of water vapor was introduced at 270 °C for 240 h (toluene concentration = 1000 ppm and SV = 20,000 mL/(g h)).

2.7. Characterization

Thermal stability test for MIL-101-Cr was performed by a Netzsch TG 209 F3 thermogravimetric analysis (TGA) under air with a ramp rate of 2 °C/min. Element contents analysis was determined by inductively coupled plasma-optical emission spectroscopy (ICP-OES). Powder X-ray diffraction (XRD) was recorded on a Panalytical X' Pert Pro diffractometer using Cu Kα radiation with a speed rate of 12°/min and step size of 0.02° in the range of $5° \leq 2\theta \leq 90°$. Raman spectra were carried out with a LabRAM Aramis Laser Raman Spectrometer employing the laser source of 532 nm with 65% of light intensity

attenuation. Transmission electron microscopy (TEM) was conducted on a JEM 2100F transmission electronic microscopy equipped with an energy dispersive spectroscopy (EDS) instruments for elemental distribution collection. The specific surface area and pore size distribution were measured by Brunauer-Emmett-Teller (BET) and Barrett-Joyner-Halenda (BJH) methods using an automated gas sorption analyzer (Quantachrome; America). X-ray photoelectron spectroscopy (XPS) measurements were recorded on a Perkin-Elmer model PHI 5600 XPS system with a monochromatic aluminum anode X-ray source ($h\nu$ = 1486.6 eV). Hydrogen temperature-programmed reduction (H_2-TPR), oxygen temperature-programmed desorption analysis (O_2-TPD), and oxygen storage capacity (OSC) were determined using a chemisorption analyzer (Quantachrome; America) equipped with a TPx system. For H_2-TPR experiments, 40 mg of samples was pretreated under argon at 300 °C for 1 h and cooled to room temperature, then it was heated from 50 to 900 °C with a rate of 10 °C/min in the 5% H_2/Ar flow (30 mL/min). And the detailed procedure for calculation of derived initial H_2 consumption rate was presented in ESI. During the O_2-TPD operation, 5% O_2/He gas mixture (30 mL/min) was introduced to samples (40 mg) from room temperature to 300 °C and maintained for 1 h; After samples being cooled down to 100 °C below, He flow (30 mL/min) was passed through the sample cell for 1 h to remove all oxygen; At last, the signals of oxygen molecule were collected by heating the samples to 900 °C under He flow with a ramp rate of 10 °C/min using a spectrometer analysis instrument (Quantachrome; America). OSC measurement was executed as follows: samples were firstly reduced by 5% H_2/Ar from room temperature to 350 °C with a rate of 10 °C/min for 1 h and then He was introduced for 1 h at this temperature. When the samples cooled down to 200 °C, 5% O_2/He mixture with a flow rate of 30 mL/min was introduced for the oxygen pulse adsorption experiment: 50 pulses were designed for oxygen adsorption. The amounts of adsorbed oxygen were calculated according to the difference between areas of pulse and calibration peaks based on the oxygen adsorption of quantitative loop of chemisorption analyzer. Because of the poor signals of H_2-TPR, O_2-TPD, and OSC, 200 mg of Cr_2O_3-C was used for signals collection. The components of fresh and used catalysts were analyzed by means of X-ray fluorescence spectrometer (XRF, Axios^{mAX}, PANalytical). *In situ* diffuse reflectance infrared Fourier transform spectroscopy (DRIFTS, Thermo Fisher Nicolet is 50, America) was used to assess the mechanism of toluene degradation. And mass spectrometer (MS, LC-D200M, TILON) was used along with the infrared spectrometer for detection of CO_2 and H_2O generated during the *in situ* DRIFTS analysis.

3. Results and discussion

3.1. Structure analysis

The XRD patterns of all samples are presented in Fig. 1(a). It is observed that the XRD diffraction peaks exhibit similar positions and are well matched with that of the standard Cr_2O_3 mode (ICSD PDF 01-070-3765), which confirm the formation of Cr_2O_3 by the pyrolysis process of precursors (see TGA curve of MIL-101-Cr, shown in Fig. S1). Compered to Cr_2O_3-C, the broader and weaker peaks are observed in XRD patterns of Cr_2O_3-M and *x*Mn/Cr_2O_3-M (Fig. 1(b)), which suggest more nano-scaled crystallites exist in the crystal [5,37]. It more easily leads to the formation of disordered structure, the occurrence of lattice defects, the exposure of inner atoms and the improvement of surface area, which are advantageous to catalytic oxidation process. It is also noted that no obvious characteristic diffraction peaks of MnO_x are obtained in all XRD patterns of xMn/Cr_2O_3-M, which is possibly ascribed to MnO_x species being incorporated in the as-prepared catalysts existed as amorphous or the diffraction peaks of MnO_x being covered by the peaks of Cr_2O_3 [38]. Actually, no MnO_x phase are detected from XRD patterns of 5, 15, 25Mn/MIL-101-Cr precursors as well (Fig. S2), where have been confirmed that MnO_x species can be produced from the reaction of $KMnO_4$ and H_2O_2.

For Raman analysis, typical peaks of Cr_2O_3-C at about 301, 340, 540 and 595 cm^{-1} are observed (Fig. 2(a)) corresponding to E_g symmetry and A_{1g} symmetry [39,40]. Notably, the most intense peak of A_{1g} occurs shift to the low wavenumber after introduction of Mn species and this shift is gradually enlarged with increasing of MnO_x amount (Fig. 2(b)), which indicates that incorporated MnO_x facilitates more lattice defects in the pyrolysis process of the precursors. Furthermore, not only position but also the intensity of peak can be strongly affected by confinement effect, defects and lattice strain [41]. It is easy to observe that all peak intensities of Cr_2O_3 become weaker especially for sample with high content of MnO_x, which imply that more lattice defects and oxygen vacancies result in the long-range disordered accumulation in the structure [25]. When the content of MnO_x is up to 25 wt%, all Raman peaks from Cr_2O_3 are nearly vanished and a new weak peak appears at 636 cm^{-1} corresponding to some vibration models of MnO_x, which possibly indicates that the excess MnO_x covers the surface of Cr_2O_3 nanocrystals.

The TEM and HRTEM images were applied to intuitively investigate the morphology of Cr_2O_3-C, Cr_2O_3-M, xMn/Cr_2O_3-M and precursors. As shown in Fig. 3(a)–(e) for TEM images, the samples derived from pyrolysis of MOF are composed of aggregation of vast small-size nanoparticles compared to Cr_2O_3-C with large-size particles, which is in accord with the XRD results of Cr_2O_3-M and xMn/Cr_2O_3-M with the broader and weaker peaks. HRTEM images of Cr_2O_3-M based samples obviously display the well-resolved lattice fringe of the *d*-spacing values at around 0.275 nm, which is confirmed from the (1 0 4) crystal plane of Cr_2O_3. The other lattice spacing (*d*) value at around 0.492 nm exists in 15 and 25Mn/Cr_2O_3-M, confirming the incorporation of MnO_x into samples as tetragonal α-MnO_2 (ICSD PDF 00-044-0141). As shown in Fig. 3(h) and (i), MnO_2 nanoparticles are tightly located on Cr_2O_3 to generate strong interaction between MnO_x and Cr_2O_3 particles, which usually enhance the synergistic effect to catalytic oxidation of VOCs [42,43]. It is more difficult to observe the existence of MnO_x in the HRTEM image of 5Mn/Cr_2O_3-M, possibly due to highly-dispersed and low loading MnO_x is embedded in Cr_2O_3 particles. When the loading content of MnO_x was up to 25%, the excess MnO_x species adhere to the surface of Cr_2O_3 (TEM image in Fig. 3(e)). It is also detected by TEM images of Mn/MIL-101-Cr precursors (Fig. S3), where MnO_x species are filled in MIL-101-Cr matrix in 5 and 15Mn/MIL-101-Cr and the isolated MnO_x species are covered on the surface of MIL-101-Cr in 25Mn/MIL-101-Cr. Element distribution images corresponding to Mn, Cr and O have been studied by high-angle annular dark-field scanning transmission electron microscopy (HAADF-STEM) and EDS. As depicted in Fig. 3(j)–(l), the overlapping of element mapping demonstrates that Mn and Cr in 5 and 15Mn/Cr_2O_3-M are uniformly distributed and it is nonuniformly distributed in 25Mn/Cr_2O_3-M. EDS results further confirm that the Mn mass fractions of 5 and 15Mn/Cr_2O_3-M are only 0.25 and 2.41 wt%, respectively (Fig. S4(a) and (b)), which are much lower than that of ICP analysis. And the Mn mass fraction of 25Mn/Cr_2O_3-M is up to 43.8% in some spots (Fig. S4(d)), which is much higher than that of ICP result. This phenomenon reveals that moderate addition of Mn species leads to uniform mutual-distribution of binary oxides with strong interaction, and excess addition results in the formation of isolated Mn-rich oxide phase after reaching to maximum mutual-distribution.

The nitrogen adsorption-desorption isotherms and pore size distributions of catalysts are shown in Fig. 4. All curves display the same type III isotherm with obvious H3 hysteresis loop, implying the existence of irregular mesoporous structure [5,44]. For Cr_2O_3-C, it is almost no adsorption/desorption occurred (see Fig. 4(a)), and it certainly give a very lower S_{BET} value (2 m^2/g) and zero pore volume value (see Table 1). The obviously improved performance of adsorption-desorption for Cr_2O_3-M derived by pyrolysis of MOF can be observed for the larger BET surface area (32 m^2/g) and pore volume (0.2 cm^3/g), which is advantageous for the diffusion of VOCs molecules and the contact

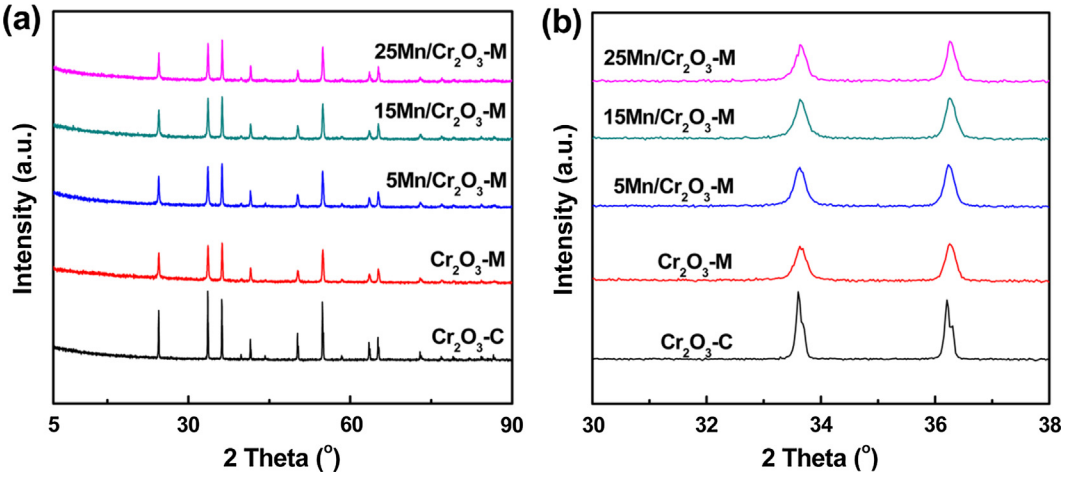

Fig. 1. Integrated (a) and enlarged region (b) of XRD patterns of the catalysts.

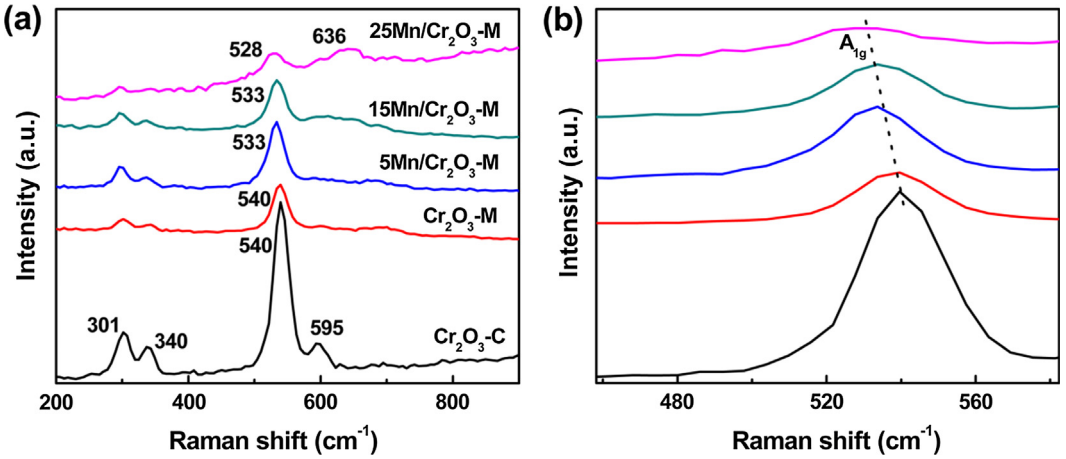

Fig. 2. Integrated (a) and partial enlarged (b) Raman patterns of catalysts.

between VOCs molecules and active sites [45,46]. After introduction of MnO_x, the specific area and pore volume of Cr_2O_3-based composites are further enlarged and show a positively-correlated tendency with increasing of the MnO_x amount. The largest BET surface area (51.8 m^2/g) and pore volume (0.4 cm^3/g) are obtained for 25Mn/Cr_2O_3-M. This phenomenon can be reasonably explained that the Mn species enter in the matrix of MIL-101-Cr in the catalyst precursors (x Mn/MIL-101-Cr), which has been confirmed by investigating BET surface areas and pore volumes of x Mn/MIL-101-Cr precursors (Fig. S5 and Table S1), then the existed MnO_x partly sustains the Cr_2O_3-M structure to avoid the excessive shrinkage in the pyrolysis. Distribution of pore diameter shown in Fig. 4(b) indicates that the mesoporous mainly exist in Cr_2O_3-M. And with increasing of MnO_x, the pore structure tends to be enlarged and irregular and the quantity of the larger pores appears to be more and obvious. It has been reported that larger porous materials are advantageous for oxidation of VOCs [17,47,48].

From Cr $2p_{3/2}$ spectra in Fig. 5(a), it can be clearly seen that the spectra of samples can be decomposed into three peaks at the binding energies of 575.7, 577, and 578.6 eV, which can be assigned to Cr^{2+}, Cr^{3+}, and Cr^{5+}, respectively [49–51]. For Mn $2p_{5/2}$ XPS spectra of 15 and 25Mn/Cr_2O_3-M in Fig. 5(b), three components at the binding energies of 640.6, 642.1, and 643.6 eV are attributed to the surface Mn^{2+}, Mn^{3+}, and Mn^{4+} in Mn-$2p_{5/2}$ orbital, respectively [25]. However, it is unconspicuous to observe Mn $2p_{5/2}$ XPS signals of 5Mn/Cr_2O_3-M, indicating the content of surface Mn species is very low. Combined with TEM analysis, it probably owes to incorporation of low-content MnO_x into the inner of Cr_2O_3 crystal and it is hard to detect inner Mn species by XPS. For comparison, the valence state of chromium ions was considered. As shown in Table 1, the higher valent Cr species of Cr_2O_3-C and Cr_2O_3-M are close to each other with about of 30% Cr^{5+} species in the samples. It is interesting that there is an obviously lower concentration of Cr ions in higher oxidation states (Cr^{5+}) for Mn-contained samples. And the quantity of Cr^{5+} is decreased with increasing of MnO_x. According to literature [52–54], MnO_x can be functionalized by the redox loop of oxidation states of manganese ions, which leads to reversible electron transfer and rapid cation diffusion. Considering the Mn $2p_{5/2}$ spectra in Fig. 5(b) and the values of Mn^{3+}/Mn^{4+} shown in Table 1, it can be concluded that the decreased quantities of Cr^{5+} is probably due to electron transfer between Cr and Mn ions caused by the strong interaction effect between MnO_x and Cr_2O_3, where electron transfer occurs from Mn to Cr ions. And it has been reported that the formation of oxygen vacancies indicates a changing of the symmetry and electronic distribution for the metallic oxide atoms [55]. Therefore, the introduction of MnO_x modifies the electronic distribution of the Cr_2O_3, which is thought to be advantageous to form oxygen vacancies and weaken the Cr-O strength [56]. Moreover, as reported before, the co-existence of virous oxidation states of chromium is favorable to the redox process which results in a better catalytic performance [57,58]. From Table 1, it can be seen that the value of Mn^{3+}/Mn^{4+} for 15Mn/Cr_2O_3-M (1.6) is higher than that of 25Mn/Cr_2O_3-M (1.4). Considering the TEM images shown in Fig. 3, where almost all of MnO_x were incorporated into the Cr_2O_3-M for 15Mn/Cr_2O_3-M, and much more isolated MnO_x particles existed in 25 Mn/Cr_2O_3-M, so the higher quantity of Mn^{3+} in 15Mn/Cr_2O_3-M is attributed to the protective effects of

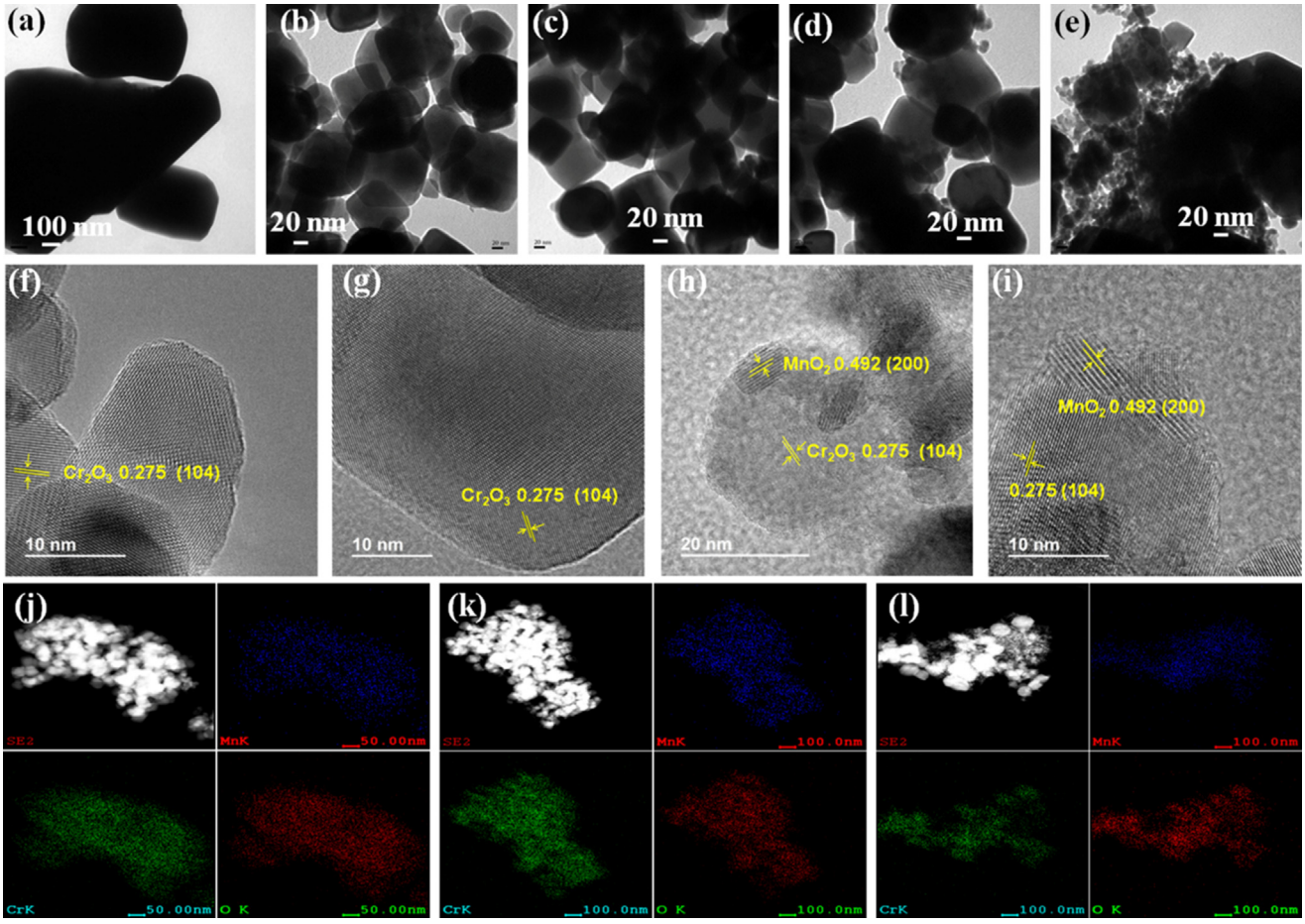

Fig. 3. TEM images of Cr_2O_3-C (a), Cr_2O_3-M (b), 5Mn/Cr_2O_3-M (c), 15Mn/Cr_2O_3-M (d), 25Mn/Cr_2O_3-M (e); HRTEM images and element mapping of catalysts: Cr_2O_3-M (f), 5Mn/Cr_2O_3-M (g) and (j), 15Mn/Cr_2O_3-M (h) and (k), 25Mn/Cr_2O_3-M (i), and (l).

Cr_2O_3 to prevent activated Mn^{3+} against being oxidized into higher valence state of Mn^{4+} in the pyrolysis process. And the high molar ratio of Mn^{3+}/Mn^{4+} is believed favorable to the formation of oxygen vacancies [31,59]. The intensity of Mn $2p_{5/2}$ spectrum for 5Mn/Cr_2O_3-M is too weak to obtain accurate quantity, thus the value of Mn^{3+}/Mn^{4+} is hardly to be confirmed, that is in accordance with analysis of TEM images.

As presented in Fig. 5(c), the O 1s XPS spectra of samples can be divided into three components with binding energies around at 530.2, 531.8, and 533.4 eV, ascribable to the surface lattice oxygen (O_{Latt}), adsorbed oxygen (O_{Ads}), and molecular water (O_{H2O}), respectively [49,60]. It is worth to consider that the ratio of O_{Latt}/O_{Ads} for the catalysts increased as follows: Cr_2O_3-C < Cr_2O_3-M < 5Mn/Cr_2O_3-M < 25Mn/Cr_2O_3-M < 15Mn/Cr_2O_3-M, which clearly shows that more surface lattice oxygen existed on Mn-contained catalysts. From element mapping analysis and HRTEM images in Fig. 3, we can conclude that the increased ratio of O_{Latt}/O_{Ads} determined by XPS is attributed to the formation of MnO_x nanoparticles in Cr_2O_3 crystal. Considering that Mn-contained catalysts have the higher catalytic activity in Fig. 8, as compared with pure Cr_2O_3 catalysts, the XPS results

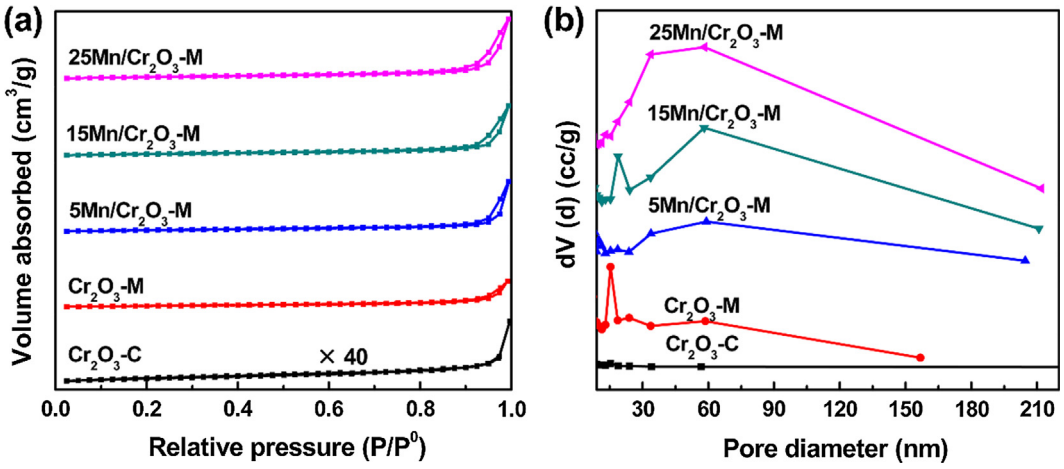

Fig. 4. Nitrogen adsorption-desorption isotherms (a) and pore size distribution (b) of catalysts.

Table 1
BET surface areas, pore volumes, average pore sizes, and surface elements composition of samples.

Samples	BET (m^2/g)	Pore volume (cm^3/g)	Average pore size (nm)	XPS		
				Cr^{5+}/Total	Mn^{3+}/Mn^{4+}	O_{Latt}/O_{Ads}
Cr_2O_3-C	2.0	0.0	18.1	0.3		1.2
Cr_2O_3-M	32.0	0.2	22.4	0.3		1.6
5Mn/Cr_2O_3-M	40.1	0.3	34.2	0.2	–[a]	2.4
15Mn/Cr_2O_3-M	43.1	0.3	31.7	0.2	1.6	5.9
25Mn/Cr_2O_3-M	51.8	0.4	31.9	0.1	1.4	4.1

[a] The intensity of XPS spectrum for 5Mn/Cr_2O_3-M is too weak to obtain accurate quantity, thus the value of Mn^{3+}/Mn^{4+} is hardly to be confirmed.

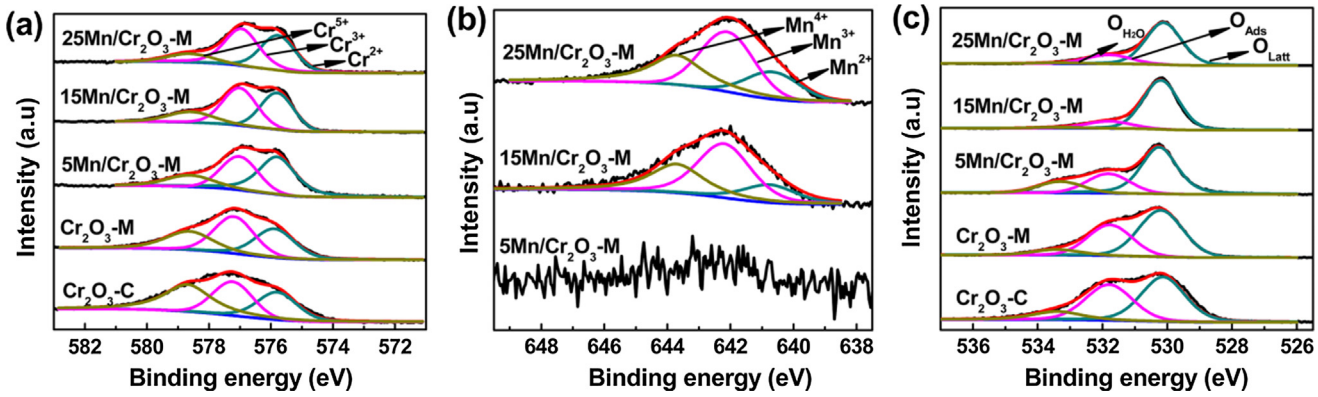

Fig. 5. XPS spectra of samples: (a) Cr $2p_{3/2}$, (b) Mn $2p_{5/2}$, and (c) O 1s.

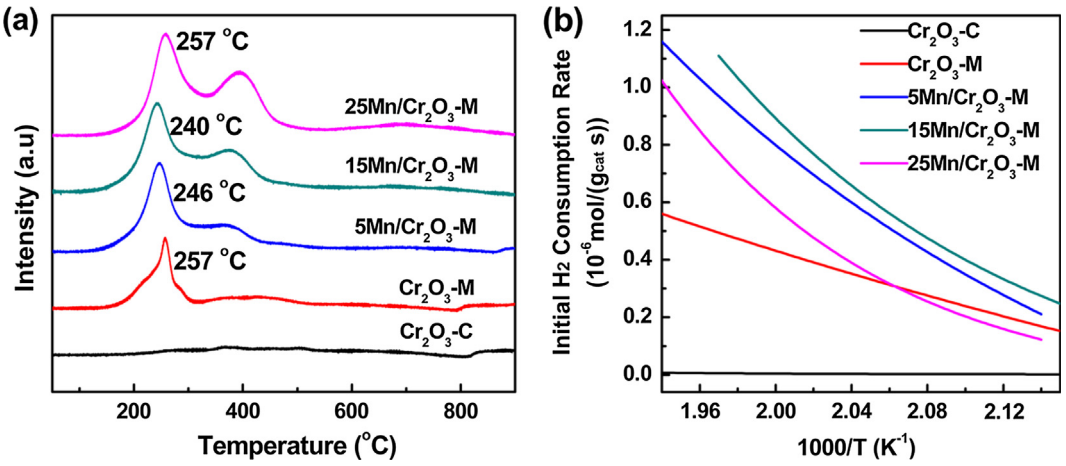

Fig. 6. H_2-TPR (a) and initial H_2 consumption rate profiles (b) of catalysts.

Table 2
Quantitative results of H_2-TPR, OSC, and O_2-TPD.

Samples	Total H_2 consumption (H_2 μmol/g)	OSC (O_2 μmol/g)	Amount of desorbed O_{Latt} in O_2-TPD (O_2 μmol/g)
Cr_2O_3-C	32.1	1.1	0
Cr_2O_3-M	475.1	40.3	0
5Mn/Cr_2O_3-M	735.7	87.1	790
15Mn/Cr_2O_3-M	849.7	169.7	864
25Mn/Cr_2O_3-M	1041.5	259.1	310

in the O 1s region indicate that surface lattice oxygen could be the most crucial factor in oxidation of toluene. The ratio of O_{Latt}/O_{Ads} for 25Mn/Cr_2O_3-M (4.1) is lower than that of 15Mn/Cr_2O_3-M (5.9). The possible explanation is that excessive crystallized MnO_x nanoparticles (Fig. 3(i)) isolated from surface of Cr_2O_3 grains when the content of MnO_x is more than 15%, therefore resulting in an improvement of adsorbed oxygen on its surface.

Fig. 6 illustrates the H_2-TPR profiles of catalysts. Two broad peaks in the range of 150–500 °C present in the reduction process of xMn/Cr_2O_3-M, implying the reduction of Cr_2O_3 and MnO_x, respectively. By analyzing H_2-TPR profile of Cr_2O_3-M, the peak centered at 257 °C is undoubtedly from the reduction of Cr_2O_3 (Cr^{5+} to Cr^{3+} and Cr^{3+} to Cr^{2+}) [61,62], thus the peak appeared at around 380 °C in H_2-TPR profiles of xMn/Cr_2O_3-M is ascribed to the reduction of MnO_x (MnO_2 to Mn_2O_3 and Mn_2O_3 to Mn_3O_4) [18,59] and its intensity is gradually enhanced with increasing of MnO_x loading. The corresponding temperature of reduction peak for Cr_2O_3 is decreased with the amount of Mn species loading and gives the lowest temperature at around 240 °C for 15Mn/Cr_2O_3-M, which manifests that the appropriate addition of Mn species is favorable to facilitate the low-temperature reducibility of Cr_2O_3 support. However, as for 25Mn/Cr_2O_3-M, its reducibility was not promoted with more addition of Mn species, which indicated that excess MnO_x could suppress the reducibility of catalysts. The total H_2 consumption

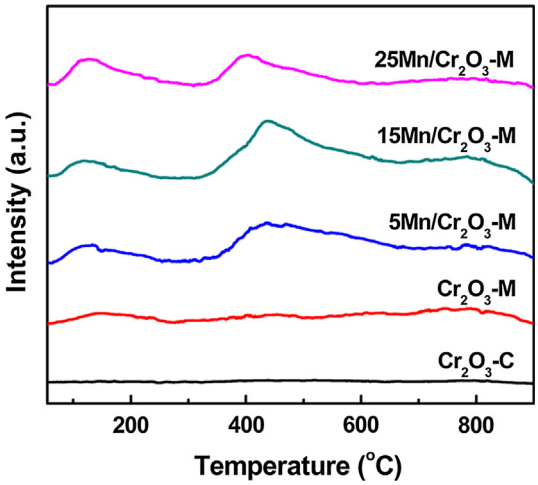

Fig. 7. O_2-TPD of catalysts.

from 50 to 900 °C for catalysts are summarized in Table 2 and the amount of hydrogen consumed implies the reducible components of catalysts. Compared to Cr_2O_3-C (32.1 μmol/g) and Cr_2O_3-M (475.1 μmol/g), the total consumption of hydrogen for xMn/Cr_2O_3-M is extremely increased, where 25Mn/Cr_2O_3-M shows the maximum value of 1041.5 μmol/g owing to higher content of MnO_x. As we know, usually, the temperature of complete catalytic oxidation of VOCs occurs below 300 °C, so initial H_2 consumption rate at low temperature is applied to evaluate the reducibility of catalysts. As shown in Fig. 6(b), the initial H_2 consumption rate of catalysts follows the sequence of Cr_2O_3-C < Cr_2O_3-M < 25Mn/Cr_2O_3-M < 5Mn/Cr_2O_3-M < 15Mn/Cr_2O_3-M. The higher initial H_2 consumption rate, the better low-temperature reducibility that normally results in higher catalytic activity [36]. OSC was performed to study the chemical absorption ability of oxygen. As shown in Table 2, the oxygen consumption of Cr_2O_3-M (40.3 μmol/g) is much more than that of Cr_2O_3-C (1.1 μmol/g), indicating more defects or oxygen vacancies exist in sample Cr_2O_3-M, which is advantageous for activated oxygen being absorbed on the surface of catalysts [36]. As for Mn-contained Cr_2O_3 catalysts (5Mn/Cr_2O_3-M and 15Mn/Cr_2O_3-M), more defects or oxygen vacancies were produced because of Cr_2O_3 crystal with disordered structure caused by incorporated MnO_x. Moreover, as the intrinsical characteristic of Mn oxide species [25], OCS of catalyst with more MnO_x can be enhanced as observed for 25Mn/Cr_2O_3-M.

O_2-TPD is an effective method to evaluate the mobility of oxygen species. As shown in Fig. 7, no obvious desorption signals appear for Cr_2O_3-C and Cr_2O_3-M in temperature range of 50–900 °C. After

Table 3
Catalytic activities and apparent activation energies (E_a) of samples with space velocity of 20,000 mL/(g h) and toluene concentration = 1000 ppm.

Samples	Space velocity	Toluene conversion and apparent activation energy			
	mL/(g h)	$T_{10\%}$ (°C)	$T_{50\%}$ (°C)	$T_{90\%}$ (°C)	E_a (kJ/mol)
Cr_2O_3-C	20,000	328	354	373	144.2
Cr_2O_3-M		272	300	310	138.9
5Mn/Cr_2O_3-M		268	291	297	132.3
15Mn/Cr_2O_3-M		248	266	268	109.7
25Mn/Cr_2O_3-M		248	264	269	110.8

introduction of MnO_x, two obvious broad peaks located at ca. 130 °C and 450 °C can be seen for xMn/Cr_2O_3-M samples, which imply the enhanced mobility of oxygen species. Generally, the peaks between 150 and 350 °C are assigned to the desorption of surface chemical oxygen, the peaks between 350 and 600 °C are from surface/subsurface lattice oxygen and the peaks above 600 °C are ascribed to bulk lattice oxygen [62–64]. Therefore, the peak centered at ca. 130 °C could be considered as physically adsorbed oxygen with impurity of surface chemical oxygen and the peak centered at ca. 450 °C is corresponding to surface/subsurface lattice oxygen. The amount of desorbed O_{Latt} in O_2-TPD was calculated and shown in Table 2. It can be seen that much more activated lattice oxygen is desorbed from 15Mn/Cr_2O_3-M than other catalysts, where this kind of lattice oxygen (surface/subsurface lattice oxygen) usually plays a crucial role in catalytic oxidation of VOCs [65,66].

3.2. Catalytic performance of catalysts

To get insights into the optimal content of MnO_x in Cr_2O_3-M, catalytic activities of catalysts for toluene oxidation were investigated under conditions of SV = 20,000 mL/(g h) and toluene concentration = 1000 ppm. As shown in Fig. 8(a), compared to Cr_2O_3-C, Cr_2O_3-M has an obviously promotion in catalytic efficiency of toluene oxidation. And the catalytic activity is further elevated by introduction of MnO_x into Cr_2O_3-M and the best catalytic activity for toluene oxidation is achieved for 15Mn/Cr_2O_3-M, which is probably attributed to the better reducibility and oxygen mobility caused by appropriate MnO_x doping. However, with further increasing of MnO_x addition, the activity is no longer extra enhanced as observed for 25Mn/Cr_2O_3-M, and actually it is slightly affected especially for high temperature (more than 270 °C). Considering characterizations such as TEM, EDS, TPR and TPD analysis, more isolated MnO_x existed in 25Mn/Cr_2O_3-M should be of no help to catalytic activity with lack of the strong interaction between MnO_x and Cr_2O_3. The temperatures of $T_{10\%}$, $T_{50\%}$, and $T_{90\%}$ for the corresponding

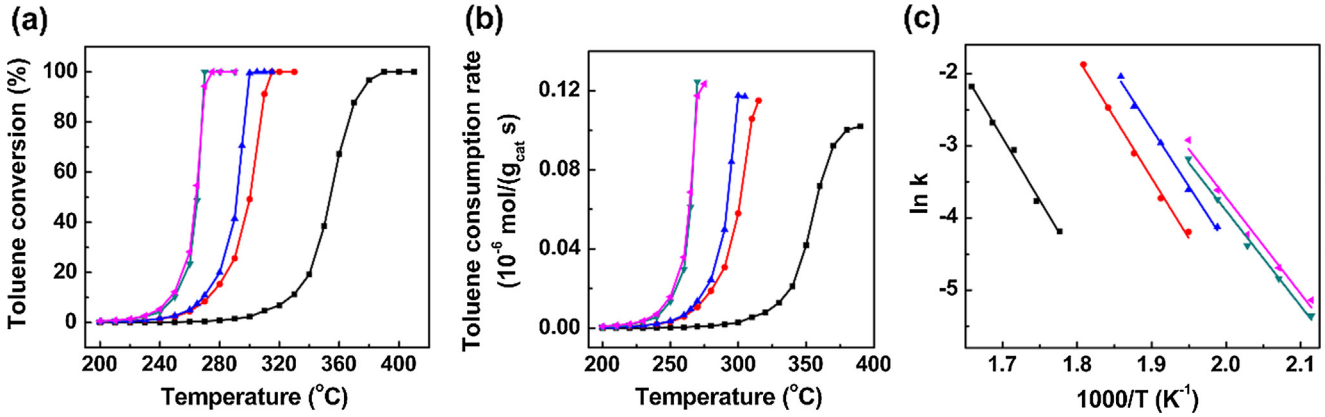

Fig. 8. Toluene conversion (A), toluene consumption rate per gram of catalyst (B), and Arrhenius plots (C) of samples with toluene concentration = 1000 ppm and SV = 20,000 mL/(g h) (Cr_2O_3-C: black line; Cr_2O_3-M: red line; 5Mn/Cr_2O_3-M: blue line; 15Mn/Cr_2O_3-M: green line; 25Mn/Cr_2O_3-M: purple line).

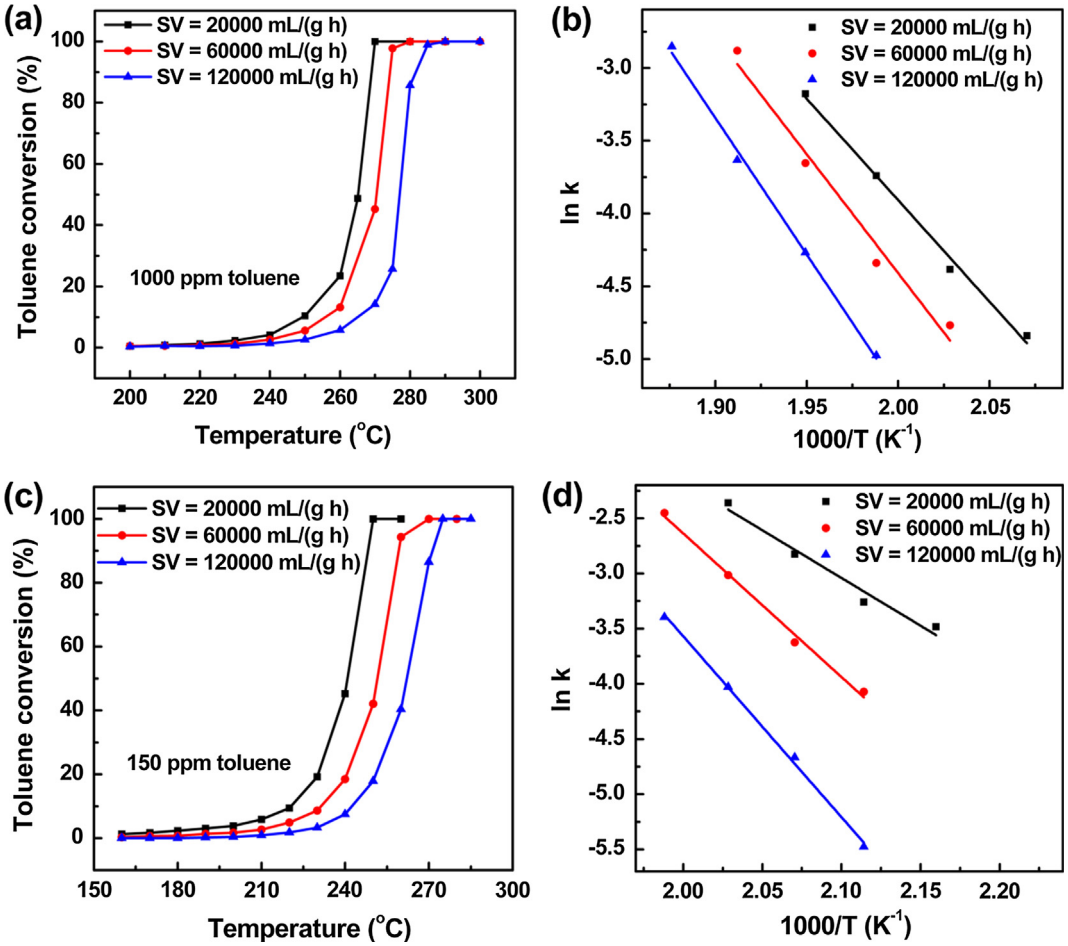

Fig. 9. Toluene conversion and Arrhenius plots of 15Mn/Cr_2O_3-M with toluene concentration = 1000 ppm (a, b) or 150 ppm (c, d), respectively at different SV.

Table 4
Catalytic activities and activation energies (E_a) of 15Mn/Cr_2O_3-M with different space velocities (20,000, 60,000, 120,000 mL/(g h)) and toluene concentrations (150 and 1000 ppm).

Concentration	Space velocity mL/(g h)	Toluene conversion and apparent activation energy			
		$T_{10\%}$ (°C)	$T_{50\%}$ (°C)	$T_{90\%}$ (°C)	E_a (kJ/mol)
1000 ppm	20,000	249	265	269	109.7
	60,000	255	270	274	135.7
	120,000	264	277	281	156.1
150 ppm	20,000	221	241	247	71.9
	60,000	231	252	259	108.2
	120,000	242	262	271	136.1

conversions are listed in Table 3, exhibiting an approximate order of the catalytic activity as follows: Cr_2O_3-C < Cr_2O_3-M < 5Mn/Cr_2O_3-M < 15Mn/Cr_2O_3-M ≈ 25Mn/Cr_2O_3-M. The toluene consumption rate of catalysts was studied, as shown in Fig. 8(b), where Cr_2O_3-M clearly displays much better performance of toluene oxidation than that of Cr_2O_3-C and it is further promoted by doping MnO_x as observed for catalytic performance of 15 and 25Mn/Cr_2O_3-M. For kinetics studies, the combustion oxidation of toluene obeys to the first-order kinetics mechanism in presence of excess oxygen, which is closely related to toluene concentration and oxygen concentration, respectively [5,36]:

$$r = -kc = [-Aexp(-E_a/RT)]c \quad (1)$$

where *r, k, A, and* E_a refer to reaction rate (μmol/(g s)), rate constant (s^{-1}), pre-exponential factor, and apparent activation energy (kJ/mol), respectively. According to the formula, Arrhenius plots can be applied to calculate activation energy (E_a) at the conversion of < 20%, which is not influenced by phase change or materials migration. As shown in Fig. 8(c) and Table 3, the E_a values decrease as follows: Cr_2O_3-C > Cr_2O_3-M > 5Mn/Cr_2O_3-M > 15Mn/Cr_2O_3-M ≈ 25Mn/Cr_2O_3-M. 15Mn/Cr_2O_3-M with the lowest E_a value exhibits the best catalytic activity for toluene oxidation.

Generally, the physicochemical properties of metal oxides caused by preparation method can result in different catalytic efficiency for VOCs degradation. Compared with Cr_2O_3-C, Cr_2O_3-M is composed of small size Cr_2O_3 nanocrystallites and exhibits three-dimensional penetrating channels, irregular mesoporosity and enhanced surface area, which are advantageous for diffusion of VOCs molecules and contact with active sites. More defects and oxygen vacancies formed in the pyrolysis process are beneficial to the catalytic activity. The introduction of MnO_x weakens the strength of Cr-O bond and facilitates the dissociation of lattice oxygen from the crystal, which provide more active oxygen and oxygen vacancies to participate catalytic reaction. Correspondingly, it causes the promotion of OSC for xMn/Cr_2O_3-M. Moreover, the enhancement of H_2 reduction capacity and initial H_2 consumption rate also confirm the efficiency to physicochemical properties via this method. However, it is worth noting that the appropriate addition amount of MnO_x is helpful to catalytic performance of toluene removal due to the strong interactions between MnO_x and Cr_2O_3, and the excessive isolated MnO_x with lack of strong interaction effect is no further promotion to catalytic activity.

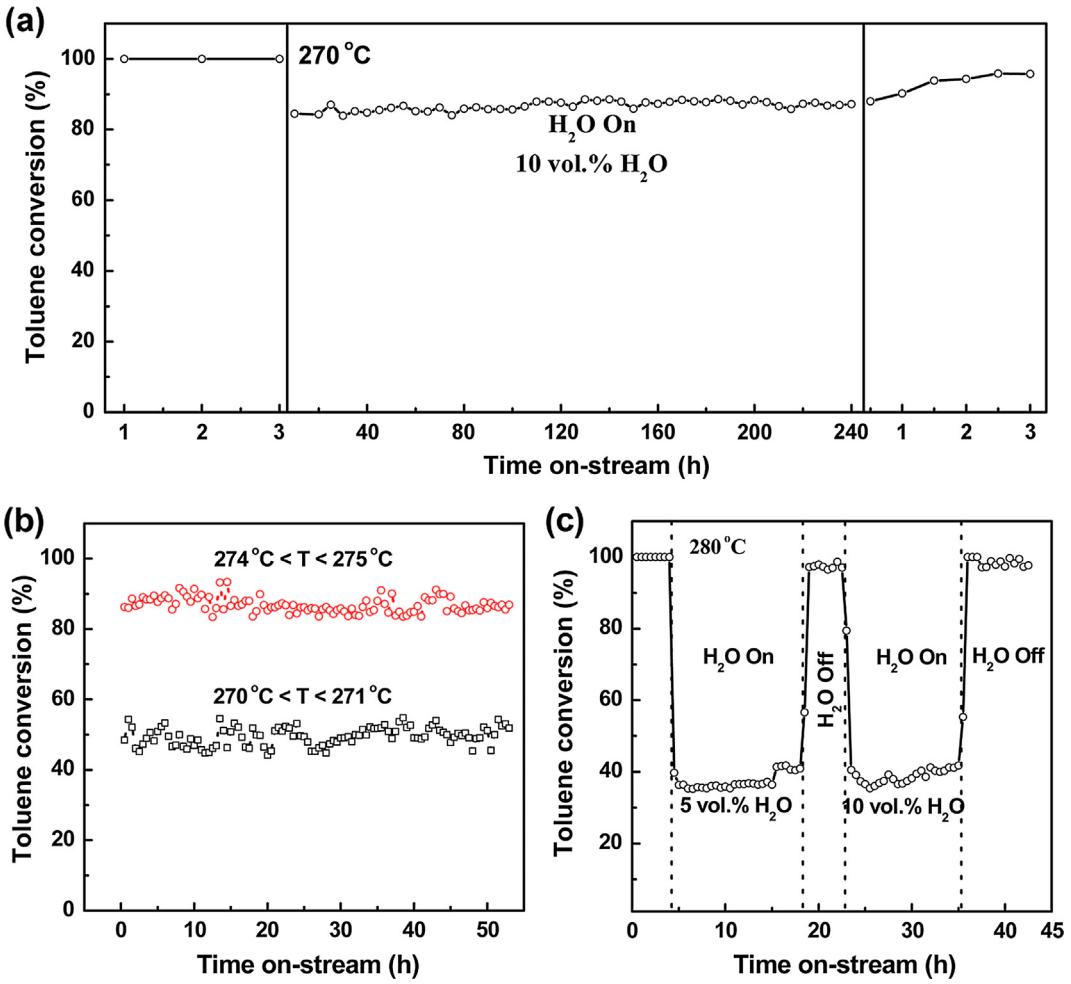

Fig. 10. Catalytic stability and durability tests. Effect of water vapor (10 vol%) on catalytic activity with toluene concentration = 1000 ppm and SV = 20,000 mL/(g h) (a), catalytic stability test with around 90% and 50% conversions (b) and effect of water vapor (5 and 10 vol%) (c) with toluene concentration = 1000 ppm and SV = 60,000 mL/(g h) over 15Mn/Cr_2O_3-M.

3.3. Effect of SV and concentration

The variation of space velocity and toluene concentration was performed to investigate the influence on catalytic activity of toluene degradation over 15Mn/Cr_2O_3-M. As shown in Fig. 9(a) and Table 4, with 1000 ppm of concentration, the catalytic oxidation of toluene on 15Mn/Cr_2O_3-M displays a tendency of deterioration accompanying the increasing of SV from 20,000 to 120,000 mL/(g h). The similar behavior was also presented for low-concentration toluene (150 ppm) with varying of SV from 20,000 to 120,000 mL/(g h) (Fig. 9(c)). Furthermore, it is obviously observed that catalytic degradation of low-concentration toluene on 15Mn/Cr_2O_3-M is easier than that of high-concentration toluene under the same conditions. The apparent activation energies (E_a) calculated by Arrhenius plots (Fig. 9(b) and (d)) indicate a positive correlation of E_a values with space velocities and toluene concentrations, which are in accordance with catalytic activities of catalyst.

3.4. Stability and durability test

To simulate realistic conditions, 10 vol% water vapor was introduced into reaction system to study catalytic stability of toluene degradation on 15Mn/Cr_2O_3-M. As shown in Fig. 10(a), toluene conversion is held on 100% at 270 °C without water vapor (toluene concentration = 1000 ppm and SV = 20,000 mL/(g h)). After introduction of 10 vol% water vapor, toluene conversion was decreased to about 85%, which indicates an inhibiting effect of water for toluene oxidation on catalyst because of the competitive adsorption of H_2O and toluene molecules on active sites. Even so, the conversion still can remain at around 85% at least for 10 days without indication of inactivation or deterioration. After turning off water vapor, the conversion can be slowly recovered within several hours to reach at around 96%. These phenomena imply that 15Mn/Cr_2O_3-M has a good stability and tolerance in the existence of water vapor and is potential for practical application. Finally, the concentrations of Cr species in fresh and used catalysts were analyzed by XRF characterization and showed the close values of 40.3 wt% and 39.8 wt% respectively, indicating the better stability of the as-prepared catalysts.

Stability test with different SV and water vapor content was also investigated on 15Mn/Cr_2O_3-M. With high SV (60,000 mL/(g h)), the conversions of toluene can be maintained at around 90% and 50% no < 50 h at 274 and 270 °C, respectively (Fig. 10(b)). The effect of water vapor under high SV (60,000 mL/(g h)) to catalytic activity over 15Mn/Cr_2O_3-M in Fig. 10(c) shows dramatically decreasing from 100% to 40% at 280 °C, which is due to high SV brings more H_2O molecules to take part in competitive adsorption on active sites of catalyst. More or less water vapor cannot further reduce toluene conversion, where it can be kept for 12 h with 5 and 10 vol% water vapor, respectively. After switching the gas flow to dry air, the conversion quickly returns to around 100%.

These results confirmed 15Mn/Cr_2O_3-M owns the excellent catalytic stability and durability with or without water vapor. It is probably

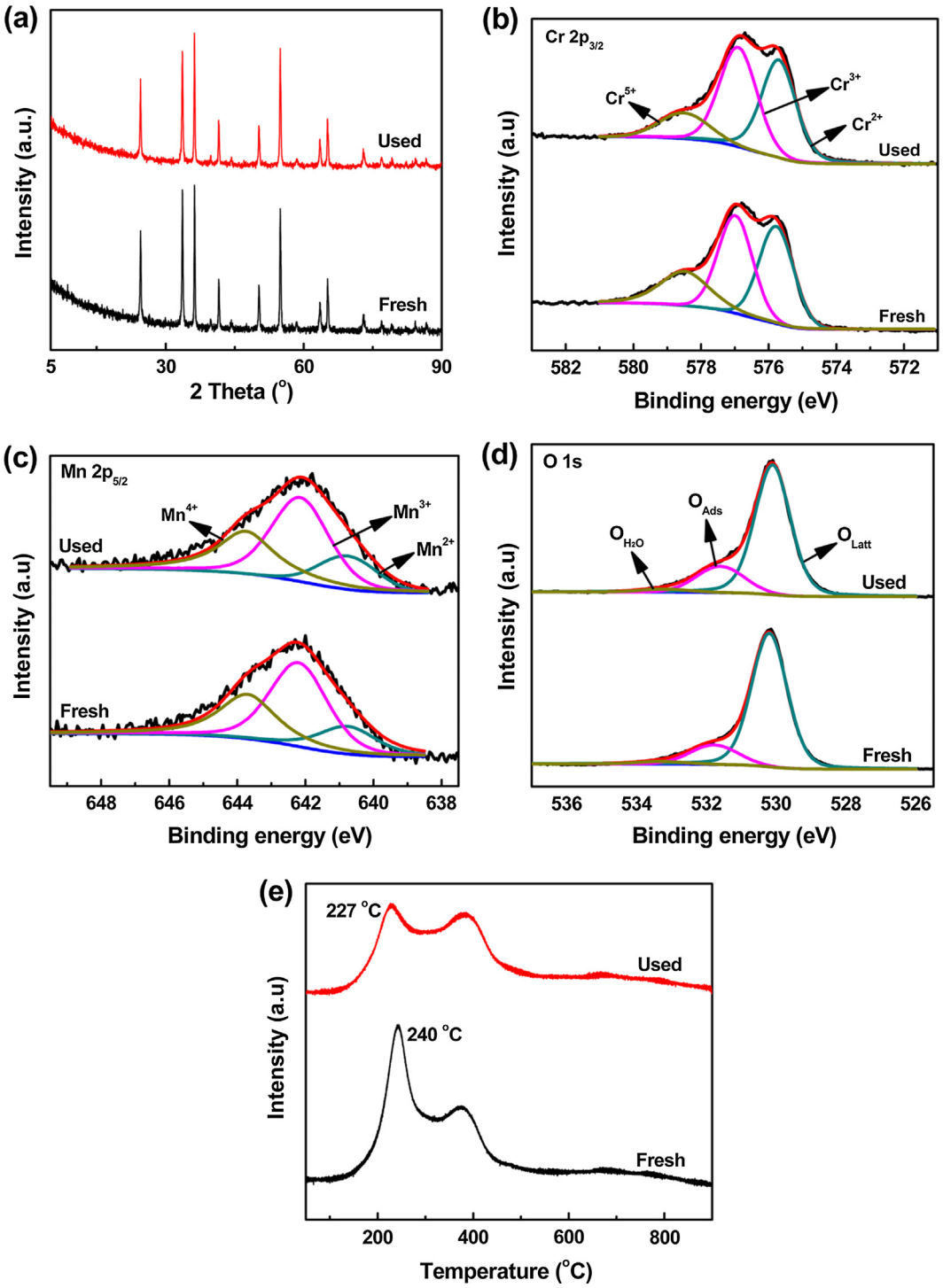

Fig. 11. XRD patterns (a), XPS spectra of Cr $2p_{3/2}$ (b), Mn $2p_{5/2}$ (c), O 1s (d), and H_2-TPR results of fresh and used 15Mn/Cr_2O_3-M.

attributed to more defects and oxygen vacancies as well irregular penetrating channels, which provide high activity and fast diffusion of reactant and product to ensure the superior coke resistance property of catalyst.

3.5. Comparison of fresh and used 15Mn/Cr_2O_3-M

To thoroughly comprehend the good tolerance and stability of 15Mn/Cr_2O_3-M, the used catalyst (240 h in 10 vol% of water vapor shown in Fig. 10(a)) was characterized by XRD, XPS, and H_2-TPR. The XRD analysis of fresh and used 15Mn/Cr_2O_3-M shows almost the same patterns, suggesting the good thermal stability of crystal structure in catalytic process (Fig. 11(a)). XPS analysis (Fig. 11(b), (c) and Table S2) exhibits that the used catalyst gives a slight decreasing of ratios for Cr^{5+}/Total and Mn^{3+}/Mn^{4+}, which could be important factors for the catalytic stability of on-stream reaction to toluene combustion [58]. Compared to fresh catalyst, O 1s XPS spectra of used 15Mn/Cr_2O_3-M give the reducing molar ratio of O_{Latt}/O_{Ads} ((Fig. 11(d) and Table S2), which is probably because some surface oxygen vacancies and defects are occupied by O_2 and H_2O to form more adsorbed oxygen during catalytic stability test. From H_2-TPR profiles in Fig. 11(e), it can be clearly seen that the first reduction peak of Cr_2O_3 is decreased and shifts

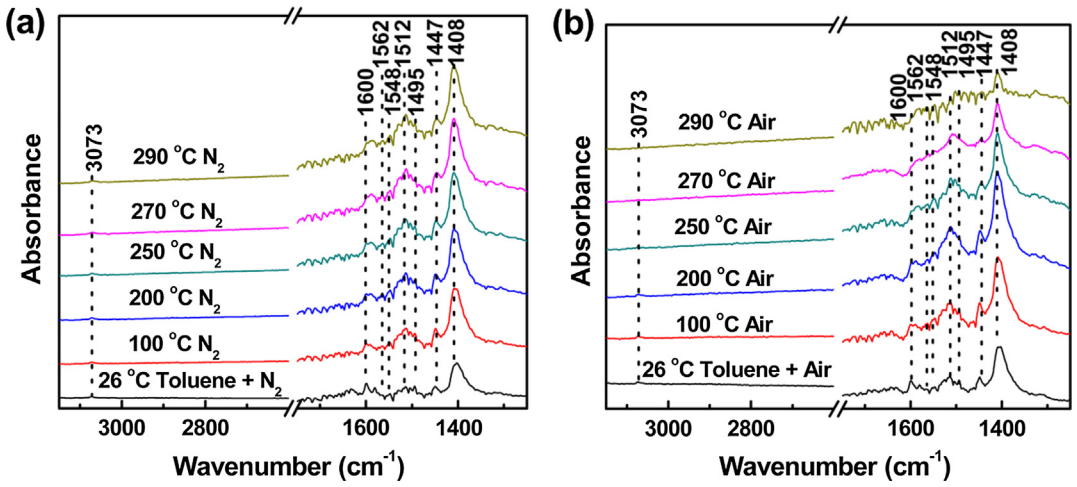

Fig. 12. *In situ* DRIFTS analysis on 15Mn/Cr_2O_3-M catalyst under exposure to toluene in N_2 (a) and air (b) at different temperatures.

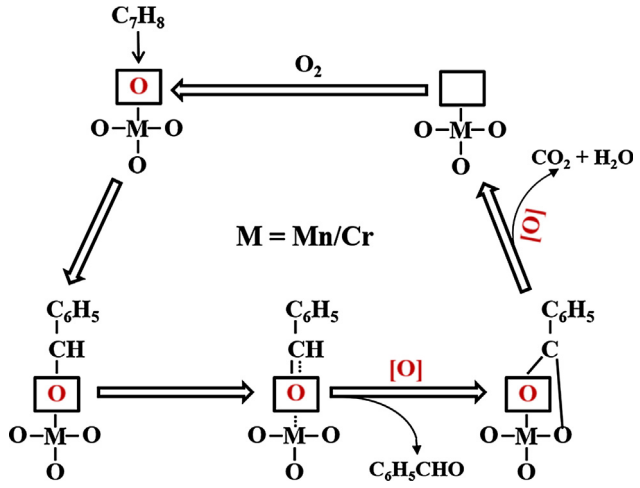

Fig. 13. Mechanism of toluene degradation over 15Mn/Cr_2O_3-M.

to lower temperature (227 °C) after being used, that is because some amount of high-valent Cr^{5+} is reduced during catalytic test. Correspondingly, the total H_2 consumption shown in Table S2 shows a reducing value for used catalyst, which derives from the variation of Cr^{5+}/Total and Mn^{3+}/Mn^{4+}. According to the characterizations, 15Mn/Cr_2O_3-M displays the better stability for crystal structure, oxygen vacancies, and reducibility in catalytic process, thus ensuring the good activity and stability for long-time catalytic evaluation of toluene oxidation.

3.6. Mechanism for degradation of toluene over 15Mn/Cr_2O_3-M

The reaction pathway for toluene oxidation on 15Mn/Cr_2O_3-M was studied by *in situ* DRIFTS analysis. To investigate the catalytic behavior of lattice oxygen, the catalyst was pre-treated in a N_2 flow at 300 °C for 2.5 h to remove absorbed oxygen and then cooled down to room temperature. Toluene was introduced using N_2 as balance gas to study transformation mechanism on the catalyst. As shown in Fig. 12(a), the characteristic absorbance bands of toluene appear at 3073 cm^{-1} for C-H stretching vibrations of the aromatic ring or methyl group and 1600, 1495, 1447 cm^{-1} for typical aromatic vibrations at low temperature [5,36]. And the bands at around 1408, 1512, and 1548 cm^{-1} are characteristics of typical carboxylate group, indicating the formation of benzoate species on the surface of catalyst. When the temperature is raised from 26 °C to 100 °C, the characteristic band of carbonate species at 1562 cm^{-1} are observed, indicating the benzoate can be transformed into carbonate species at higher temperature [67]. Further raise the temperature to 290 °C, the intensity of intermediates is enhanced continuously and finally reach to saturation. It is worth noting that N_2 was continuously introduced into the reaction system until analysis was finished. The results proved that surface lattice oxygen on catalyst can participate in oxidation of adsorbed toluene to form intermediate species but it is not enough to deeply mineralize intermediate species due to the lack of sustainable supply of activated oxygen. As a comparison, the similar reaction was carried out in air flow to investigate transformation mechanism with gas-phase oxygen. As shown in Fig. 12(b) for DRIFTS analysis, the band intensity of benzoate species is gradually strengthened with temperature increasing from 26 to 200 °C, indicating that introduction of gas-phase oxygen cannot facilitate the transformation of toluene below 200 °C. When the temperature is above 200 °C, the intensities of all bands are gradually decreased to finally almost vanish at 290 °C. It indicates that O_2 can effectively promote decomposition of intermediates by converting gas-phase oxygen into surface activated lattice oxygen. Further, MS was used to monitor CO_2 and H_2O generated during the *in situ* DRIFTS analysis at 26 and 290 °C, respectively. Based on *in situ* DRIFTS and MS results, the pathway for catalytic oxidation of toluene on 15Mn/Cr_2O_3-M is possibly *via* rapid transformation to benzoate species and finally form CO_2 and H_2O (see MS results in Fig. S6), as shown in Fig. 13, where the corresponding bands of aldehydic species cannot be obviously observed, implying rapidly transformation from aldehydic species to benzoate species [68].

4. Conclusion

In summary, the xMn/Cr_2O_3-M catalysts were synthesized by combination methods of impregnation and *in situ* redox precipitation and then pyrolysis. The introduction of MnO_x into Cr_2O_3 can enhance the reducibility, oxygen storage capacity and oxygen mobility due to the generated more oxygen vacancies and defects as well strong interaction between two metal oxides, which are favorable to oxidation of VOCs. The 15Mn/Cr_2O_3-M catalyst is observed to present the best catalytic performance under different SV and concentrations. Under on-stream test with 10 vol% water vapor, 15Mn/Cr_2O_3-M displays the good catalytic stability with 85% of toluene conversion at least for 240 h, which could be ascribed to more stable physicochemical properties during catalytic test. These results highlight the achievement of MOFs-deriving mixed metal oxides as the efficient and stable catalyst for VOCs catalytic degradation.

Acknowledgements

This work was supported by “Cooperation of Industry-University-

Institute and Scientific and Technological Cooperation" of Xiamen [No. 3502Z20172029 and 3502Z20182006]; the "One Hundred Talent Project" from Chinese Academy of Sciences; the "Key Research Program of Frontier Sciences" from Chinese Academy of Sciences [No. QYZDB-SSW-DQC022] and National Natural Science Foundation of China [No. 21501175].w

Appendix A. Supplementary material

Supplementary data to this article can be found online at https://doi.org/10.1016/j.apsusc.2018.12.277.

References

[1] M.S. Kamal, S.A. Razzak, M.M. Hossain, Catalytic oxidation of volatile organic compounds (VOCs) – a review, Atmos. Environ. 140 (2016) 117–134.
[2] J. Chen, X. Chen, X. Chen, W. Xu, Z. Xu, H. Jia, J. Chen, Homogeneous introduction of CeO_y into MnOx-based catalyst for oxidation of aromatic VOCs, Appl. Catal. B 224 (2018) 825–835.
[3] P.V. Shanbhag, A.K. Guha, K.K. Sirkar, Membrane-based integrated absorption−oxidation reactor for destroying VOCs in air, Environ. Sci. Technol. 30 (1996) 3435–3440.
[4] C. Zhang, C. Wang, W. Zhan, Y. Guo, Y. Guo, G. Lu, A. Baylet, A. Giroir-Fendler, Catalytic oxidation of vinyl chloride emission over $LaMnO_3$ and $LaB_{0.2}Mn_{0.8}O_3$ (B = Co, Ni, Fe) catalysts, Appl. Catal. B 129 (2013) 509–516.
[5] X. Chen, X. Chen, S. Cai, J. Chen, W. Xu, H. Jia, J. Chen, Catalytic combustion of toluene over mesoporous Cr_2O_3-supported platinum catalysts prepared by in situ pyrolysis of MOFs, Chem. Eng. J. 334 (2018) 768–779.
[6] W.B. Li, J.X. Wang, H. Gong, Catalytic combustion of VOCs on non-noble metal catalysts, Catal. Today 148 (2009) 81–87.
[7] X. Weng, P. Sun, Y. Long, Q. Meng, Z. Wu, Catalytic oxidation of chlorobenzene over $Mn_xCe_{1-x}O_2$/HZSM-5 catalysts: a study with practical implications, Environ. Sci. Technol. 51 (2017) 8057–8066.
[8] T. Garcia, S. Agouram, J.F. Sánchez-Royo, R. Murillo, A.M. Mastral, A. Aranda, I. Vázquez, A. Dejoz, B. Solsona, Deep oxidation of volatile organic compounds using ordered cobalt oxides prepared by a nanocasting route, Appl. Catal. A 386 (2010) 16–27.
[9] B. Bai, H. Arandiyan, J. Li, Comparison of the performance for oxidation of formaldehyde on nano-Co_3O_4, 2D-Co_3O_4, and 3D-Co_3O_4 catalysts, Appl. Catal. B 142–143 (2013) 677–683.
[10] B. de Rivas, R. López-Fonseca, C. Jiménez-González, J.I. Gutiérrez-Ortiz, Synthesis, characterisation and catalytic performance of nanocrystalline Co_3O_4 for gas-phase chlorinated VOC abatement, J. Catal. 281 (2011) 88–97.
[11] S.C. Kim, W.G. Shim, Recycling the copper based spent catalyst for catalytic combustion of VOCs, Appl. Catal. B 79 (2008) 149–156.
[12] P. Yang, S. Yang, Z. Shi, Z. Meng, R. Zhou, Deep oxidation of chlorinated VOCs over CeO_2-based transition metal mixed oxide catalysts, Appl. Catal. B 162 (2015) 227–235.
[13] P. Yang, Z. Meng, S. Yang, Z. Shi, R. Zhou, Highly active behaviors of CeO_2–CrO_x mixed oxide catalysts in deep oxidation of 1,2-dichloroethane, J. Mol. Catal. A: Chem. 393 (2014) 75–83.
[14] M. Piumetti, D. Fino, N. Russo, Mesoporous manganese oxides prepared by solution combustion synthesis as catalysts for the total oxidation of VOCs, Appl. Catal. B 163 (2015) 277–287.
[15] S.C. Kim, W.G. Shim, Catalytic combustion of VOCs over a series of manganese oxide catalysts, Appl. Catal. B 98 (2010) 180–185.
[16] F. Wang, H. Dai, J. Deng, G. Bai, K. Ji, Y. Liu, Manganese oxides with rod-, wire-, tube-, and flower-like morphologies: highly effective catalysts for the removal of toluene, Environ. Sci. Technol. 46 (2012) 4034–4041.
[17] Y. Liu, H. Dai, J. Deng, L. Zhang, Z. Zhao, X. Li, Y. Wang, S. Xie, H. Yang, G. Guo, Controlled generation of uniform spherical $LaMnO_3$, $LaCoO_3$, Mn_2O_3, and Co_3O_4 nanoparticles and their high catalytic performance for carbon monoxide and toluene oxidation, Inorg. Chem. 52 (2013) 8665–8676.
[18] B. Bai, J. Li, J. Hao, 1D-MnO_2, 2D-MnO_2 and 3D-MnO_2 for low-temperature oxidation of ethanol, Appl. Catal. B 164 (2015) 241–250.
[19] A.K. Sinha, K. Suzuki, Three-dimensional mesoporous chromium oxide: a highly efficient material for the elimination of volatile organic compounds, Angew. Chem. Int. Ed. 44 (2005) 271–273.
[20] Y. Wang, X. Yuan, X. Liu, J. Ren, W. Tong, Y. Wang, G. Lu, Mesoporous single-crystal Cr_2O_3: synthesis, characterization, and its activity in toluene removal, Solid State Sci. 10 (2008) 1117–1123.
[21] C.M. Pradier, F. Rodrigues, P. Marcus, M.V. Landau, M.L. Kaliya, A. Gutman, M. Herskowitz, Supported chromia catalysts for oxidation of organic compounds: the state of chromia phase and catalytic performance, Appl. Catal. B 27 (2000) 73–85.
[22] H. Rotter, M.V. Landau, M. Herskowitz, Combustion of chlorinated VOC on nanostructured chromia aerogel as catalyst and catalyst support, Environ. Sci. Technol. 39 (2005) 6845–6850.
[23] H. Rotter, M.V. Landau, M. Carrera, D. Goldfarb, M. Herskowitz, High surface area chromia aerogel efficient catalyst and catalyst support for ethylacetate combustion, Appl. Catal. B 47 (2004) 111–126.
[24] J.J. Carey, M. Legesse, M. Nolan, Low valence cation doping of bulk Cr_2O_3: charge compensation and oxygen vacancy formation, J. Phys. Chem. C 120 (2016) 19160–19174.
[25] J. Chen, X. Chen, W. Xu, Z. Xu, J. Chen, H. Jia, J. Chen, Hydrolysis driving redox reaction to synthesize Mn-Fe binary oxides as highly active catalysts for the removal of toluene, Chem. Eng. J. 330 (2017) 281–293.
[26] A. Kanyaporn, O.S. Mi, A.D. Adjei, J. Xiaoyan, J. Nutpaphat, K.I. Young, S. Thapanee, K. Yong-Mook, H. Seong-Ju, Holey 2D nanosheets of low-valent manganese oxides with an excellent oxygen catalytic activity and a high functionality as a catalyst for Li-O_2 batteries, Adv. Funct. Mater. 28 (2018) 1–11.
[27] B. Liu, Y. Zhang, J. Wang, M. Lu, Z. Peng, G. Li, T. Jiang, Investigations on the MnO_2-Fe_2O_3 system roasted in air atmosphere, Adv. Powder Technol. 28 (2017) 2167–2176.
[28] T. Mishra, P. Mohapatra, K.M. Parida, Synthesis, characterisation and catalytic evaluation of iron–manganese mixed oxide pillared clay for VOC decomposition reaction, Appl. Catal. B 79 (2008) 279–285.
[29] D.A. Aguilera, A. Perez, R. Molina, S. Moreno, Cu–Mn and Co–Mn catalysts synthesized from hydrotalcites and their use in the oxidation of VOCs, Appl. Catal. B 104 (2011) 144–150.
[30] Z. Chen, Q. Yang, H. Li, X. Li, L. Wang, S. Chi Tsang, Cr–MnO_x mixed-oxide catalysts for selective catalytic reduction of NO_x with NH_3 at low temperature, J. Catal. 276 (2010) 56–65.
[31] M. Baldi, V.S. Escribano, J.M.G. Amores, F. Milella, G. Busca, Characterization of manganese and iron oxides as combustion catalysts for propane and propene, Appl. Catal. B 17 (1998) 175–182.
[32] M.R. Morales, B.P. Barbero, L.E. Cadús, Combustion of volatile organic compounds on manganese iron or nickel mixed oxide catalysts, Appl. Catal. B 74 (2007) 1–10.
[33] R. Das, P. Pachfule, R. Banerjee, P. Poddar, Metal and metal oxide nanoparticle synthesis from metal organic frameworks (MOFs): finding the border of metal and metal oxides, Nanoscale 4 (2012) 591–599.
[34] S.-N. Zhao, X.-Z. Song, S.-Y. Song, H.-J. Zhang, Highly efficient heterogeneous catalytic materials derived from metal-organic framework supports/precursors, Coord. Chem. Rev. 337 (2017) 80–96.
[35] F. Ashouri, M. Zare, M. Bagherzadeh, Manganese and cobalt-terephthalate metal-organic frameworks as a precursor for synthesis of Mn_2O_3, Mn_3O_4 and Co_3O_4 nanoparticles: active catalysts for olefin heterogeneous oxidation, Inorg. Chem. Commun. 61 (2015) 73–76.
[36] X. Chen, X. Chen, E. Yu, S. Cai, H. Jia, J. Chen, P. Liang, In situ pyrolysis of Ce-MOF to prepare CeO_2 catalyst with obviously improved catalytic performance for toluene combustion, Chem. Eng. J. 344 (2018) 469–479.
[37] X. Liu, J. Wang, J. Zeng, X. Wang, T. Zhu, Catalytic oxidation of toluene over a porous Co_3O_4-supported ruthenium catalyst, RSC Adv. 5 (2015) 52066–52071.
[38] M. Martins, J. Milikić, B. Šljukić, G.S.P. Soylu, A.B. Yurtcan, G. Bozkurt, D.M.F. Santos, Mn_2O_3-MO (MO = ZrO_2, V_2O_5, WO_3) supported PtNi nanoparticles: designing stable and efficient electrocatalysts for oxygen reduction and borohydride oxidation, Microporous Mesoporous Mater. 273 (2019) 286–293.
[39] M. Roy, S. Ghosh, M.K. Naskar, Solvothermal synthesis of Cr_2O_3 nanocubes via template-free route, Mater. Chem. Phys. 159 (2015) 101–106.
[40] J. Mougin, T. Le Bihan, G. Lucazeau, High-pressure study of Cr_2O_3 obtained by high-temperature oxidation by X-ray diffraction and Raman spectroscopy, J. Phys. Chem. Solids 62 (2001) 553–563.
[41] K.K. Mandari, J.Y. Do, A.K.R. Police, M. Kang, Natural solar light-driven preparation of plasmonic resonance-based alloy and core-shell catalyst for sustainable enhanced hydrogen production: green approach and characterization, Appl. Catal. B 231 (2018) 137–150.
[42] F. Liu, S. Zuo, X. Xia, J. Sun, Y. Zou, L. Wang, C. Li, C. Qi, Generalized and high temperature synthesis of a series of crystalline mesoporous metal oxides based nanocomposites with enhanced catalytic activities for benzene combustion, J. Mater. Chem. A 1 (2013) 4089–4096.
[43] C. Liu, H. Xian, Z. Jiang, L. Wang, J. Zhang, L. Zheng, Y. Tan, X. Li, Insight into the improvement effect of the Ce doping into the SnO_2 catalyst for the catalytic combustion of methane, Appl. Catal. B 176–177 (2015) 542–552.
[44] S. Maiti, A. Pramanik, S. Mahanty, Electrochemical energy storage in Mn_2O_3 porous nanobars derived from morphology-conserved transformation of benzene-tricarboxylate-bridged metal-organic framework, CrystEngComm. 18 (2016) 450–461.
[45] Y. Xia, H. Dai, H. Jiang, J. Deng, H. He, C.T. Au, Mesoporous chromia with ordered three-dimensional structures for the complete oxidation of toluene and ethyl acetate, Environ. Sci. Technol. 43 (2009) 8355–8360.
[46] Y.T. Lai, T.C. Chen, Y.K. Lan, B.S. Chen, J.H. You, C.M. Yang, N.C. Lai, J.H. Wu, C.S. Chen, Pt/SBA-15 as a highly efficient catalyst for catalytic toluene oxidation, ACS Catal. 4 (2014) 3824–3836.
[47] Z. Wu, J. Deng, Y. Liu, S. Xie, Y. Jiang, X. Zhao, J. Yang, H. Arandiyan, G. Guo, H. Dai, Three-dimensionally ordered mesoporous Co_3O_4-supported Au–Pd alloy nanoparticles: high-performance catalysts for methane combustion, J. Catal. 332 (2015) 13–24.
[48] T. Barakat, J.C. Rooke, H.L. Tidahy, M. Hosseini, R. Cousin, J.F. Lamonier, J.M. Giraudon, G.D. Weireld, B.L. Su, S. Siffert, Noble-metal-based catalysts supported on zeolites and macro-mesoporous metal oxide supports for the total oxidation of volatile organic compounds, ChemSusChem 4 (2011) 1420–1430.
[49] L. Marchetti, F. Miserque, S. Perrin, M. Pijolat, XPS study of Ni-base alloys oxide films formed in primary conditions of pressurized water reactor, Surf. Interface Anal. 47 (2015) 632–642.
[50] F. Cavani, M. Koutyrev, F. Trifirò, A. Bartolini, D. Ghisletti, R. Iezzi, A. Santucci, G. Del Piero, Chemical and physical characterization of alumina-supported chromia-based catalysts and their activity in dehydrogenation of isobutane, J. Catal.

158 (1996) 236–250.
[51] B.M. Weckhuysen, I.E. Wachs, R.A. Schoonheydt, Surface chemistry and spectroscopy of chromium in inorganic oxides, Chem. Rev. 96 (1996) 3327–3350.
[52] H. Li, T. Huang, Y. Lu, L. Cui, Z. Wang, C. Zhang, S. Lee, Y. Huang, J. Cao, W. Ho, Unraveling the mechanisms of room-temperature catalytic degradation of indoor formaldehyde and its biocompatibility on colloidal TiO_2-supported MnO_x–CeO_2, Environ. Sci: Nano 5 (2018) 1130–1139.
[53] H. Xu, N. Yan, Z. Qu, W. Liu, J. Mei, W. Huang, S. Zhao, Gaseous heterogeneous catalytic reactions over Mn-based oxides for environmental applications: a critical review, Environ. Sci. Technol. 51 (2017) 8879–8892.
[54] Y. Meng, W. Song, H. Huang, Z. Ren, S.-Y. Chen, S.L. Suib, Structure-property relationship of bifunctional MnO_2 nanostructures: highly efficient, ultra-stable electrochemical water oxidation and oxygen reduction reaction catalysts identified in alkaline media, J. Am. Chem. Soc. 136 (2014) 11452–11464.
[55] M.V. Ganduglia-Pirovano, A. Hofmann, J. Sauer, Oxygen vacancies in transition metal and rare earth oxides: current state of understanding and remaining challenges, Surf. Sci. Rep. 62 (2007) 219–270.
[56] W. Zhong, M. Liu, J. Dai, J. Yang, L. Mao, D. Yin, Synergistic hollow CoMo oxide dual catalysis for tandem oxygen transfer: preferred aerobic epoxidation of cyclohexene to 1,2-epoxycyclohexane, Appl. Catal. B 225 (2018) 180–196.
[57] A.K. Sinha, K. Suzuki, Three-dimensional mesoporous chromium oxide: a highly efficient material for the elimination of volatile organic compounds, Angew. Chem. Int. Ed. 44 (2005) 271–273.
[58] A.K. Sinha, K. Suzuki, Novel mesoporous chromium oxide for VOCs elimination, Appl. Catal. B 70 (2007) 417–422.
[59] D. Delimaris, T. Ioannides, VOC oxidation over MnO_x-CeO_2 catalysts prepared by a combustion method, Appl. Catal. B 84 (2008) 303–312.
[60] M.C. Biesinger, C. Brown, J.R. Mycroft, R.D. Davidson, N.S. McIntyre, X-ray photoelectron spectroscopy studies of chromium compounds, Surf. Interface Anal. 36 (2004) 1550–1563.
[61] G. Bai, H. Dai, Y. Liu, K. Ji, X. Li, S. Xie, Preparation and catalytic performance of cylinder-and cake-like Cr_2O_3 for toluene combustion, Catal. Commun. 36 (2013) 43–47.
[62] J.S.B. Grzybowska, R. Grabowski, K. Wcisło, A. Kozłowska, J. Stoch, J. Zieliński, Chromium oxide/alumina catalysts in oxidative dehydrogenation of isobutane, J. Catal. 178 (1998) 687–700.
[63] L. Zhong, W. Cai, Y. Yu, Q. Zhong, Insights into synergistic effect of chromium oxides and ceria supported on Ti-PILC for NO oxidation and their surface species study, Appl. Surf. Sci. 325 (2015) 52–63.
[64] W.L. Wang, Q. Meng, Y. Xue, X. Weng, P. Sun, Z. Wu, Lanthanide perovskite catalysts for oxidation of chloroaromatics: secondary pollution and modifications, J. Catal. 366 (2018) 213–222.
[65] Z. Hou, J. Feng, T. Lin, H. Zhang, X. Zhou, Y. Chen, The performance of manganese-based catalysts with $Ce_{0.65}Zr_{0.35}O_2$ as support for catalytic oxidation of toluene, Appl. Surf. Sci. 434 (2018) 82–90.
[66] W. Si, Y. Wang, S. Zhao, F. Hu, J. Li, A facile method for in situ preparation of the MnO_2/$LaMnO_3$ catalyst for the removal of toluene, Environ. Sci. Technol. 50 (2016) 4572–4578.
[67] S.B. Kang, S.B. Nam, B.K. Cho, I.-S. Nam, C.H. Kim, S.H. Oh, Effect of speciated HCs on the performance of modern commercial TWCs, Catal. Today 231 (2014) 3–14.
[68] S. Zhao, K. Li, S. Jiang, J. Li, Pd–Co based spinel oxides derived from pd nanoparticles immobilized on layered double hydroxides for toluene combustion, Appl. Catal. B 181 (2016) 236–248.